Exceptional points in cylindrical elastic media with radiation loss

Kei Matsushima [*], Yuki Noguchi, and Takayuki Yamada

Department of Mechanical Engineering, Graduate School of Engineering, the University of Tokyo,
2-11-16 Yayoi, Bunkyo-ku, Tokyo 113-8656, Japan

Exceptional points (EPs) are singular points on a parameter space at which some eigenvalues (scattering poles) and their corresponding eigenmodes coalesce. This study shows the existence of second- and third-order EPs in cylindrical elastic systems with radiation loss. We consider multilayered cylindrical solids under the plane-strain condition placed in a background elastic or acoustic medium. Elastic and acoustic waves propagating in the background media experience radiation loss. We optimize the radii and the material constants of the multilayered solids, such that some scattering poles coalesce on the complex frequency plane. Some numerical experiments are performed to confirm that the coalescence originates from EPs. We expect that this study provides a new approach for enhancing mechanical sensors.

I. INTRODUCTION

Exceptional points (EPs) are singularities in a parameter space at which both eigenvalues and eigenmodes coalesce [1–3]. This simultaneous degeneracy is a unique phenomenon of non-Hermitian systems. Unlike Hermitian systems, non-Hermitian systems have complex eigenvalues, and their imaginary part represents the rate of exponential decay or divergence of resonances in time. Around an EP, two (or more) eigenvalues are associated with each other and draw a Riemann surface of a multivalued root function on the parameter space. This special structure can be observed by continuously changing the parameters around an EP and tracking the corresponding eigenvalues, called EP encircling [4]. As the rootlike behavior improves the sensitivity of the eigenvalue splitting, a promising application of the non-Hermitian degeneracy is the enhancement of optical and mechanical sensors [5–11].

Parity-time (PT) symmetry is one of the most successful approaches for realizing EPs [12–15]. A system is said to be PT symmetric if the same amount of gain and loss is symmetrically distributed in space. Due to these gain and loss, PT-symmetric systems are non-Hermitian and possibly exhibit EPs. If a system is PT symmetric, the non-Hermitian degeneracy occurs at the PT phase transition points, which can be easily found by tuning the amount of gain and loss [16].

Although the PT symmetry is an important property when discussing non-Hermitian physics, the EP itself is ubiquitous for various non-Hermitian systems. For example, dielectric microcavities can induce the non-Hermitian degeneracy without gain by tuning the dielectric constant and/or the system geometry [17]. Kullig *et al.* recently showed the existence of second- and third-order EPs in two-dimensional multilayered microdisk cavities [18]. They optimized the radii and refractive indices of the layered cavities such that two or three whispering gallary modes coalesce at a single complex

frequency. Bulgakov *et al.* proved that a spheroid exhibits a second-order EP [19]. Abdrabou and Lu studied EPs that arise in two-dimensional multiple scattering systems [20]. Meanwhile, Gwak *et al.* realized steady EPs by deforming circular microcavity [21]. Photonic crystal slabs also exhibit EPs without material gain [22–26].

EPs can also be observed in acoustic and elastic systems. As mentioned, PT symmetry is a convenient platform for discussing non-Hermitian effects on acoustic and elastic wave propagation. Recent studies revealed that the well-known anomalies of PT symmetric systems (e.g., phase transition, asymmetrical reflectance, lasing/antilasing, negative refraction, and enhanced sensitivity) are observed in such systems [27–41]. However, the existence of EPs in two- and three-dimensional passive elastic systems is still uncertain, except for an open periodic system [42].

In this study, we numerically show that second- and third-order EPs exist in cylindrical elastic media without gain. The system comprises a multilayered cylindrical solid and background elastic or acoustic medium. The background medium is unbounded in space and induces the energy loss due to the radiation in the radial direction. The solid-solid and solid-fluid coupled problems are solved via Helmholtz decomposition and cylindrical functions. Following Ref. [18], we optimize the radii and material constants such that two or three eigenvalues (scattering poles) coalesce on the complex frequency plane. Subsequently, the EP encircling is performed around the optimized parameters to confirm that the coalescence originates from the non-Hermitian degeneracy. Moreover, we show that the degenerate poles behave as multivalued root functions around EPs, which is an important property for enhancing mechanical sensors.

II. MODEL

We consider the time-harmonic oscillation of a multilayered solid embedded in a background elastic or acoustic medium as shown in Fig. 1. Each solid layer, indexed by
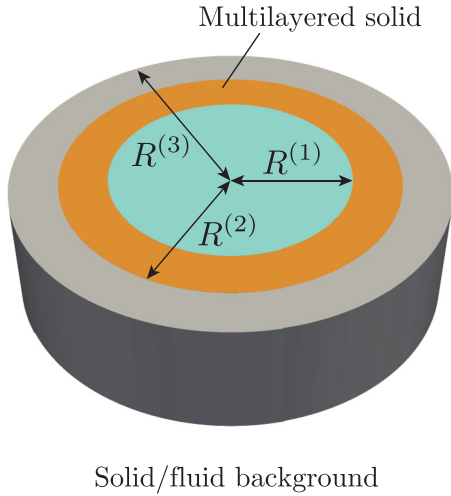
*matsushima@mech.t.u-tokyo.ac.jp

144104-1

FIG. 1. Multilayered elastic solid embedded in an elastic or acoustic medium. The figure illustrates the case of $N = 3$.

the integer $l = 1, \ldots, N$ (from innermost to outermost), is a linear, homogeneous, and isotropic elastic medium with mass density $\rho^{(l)}$ and Lamé constants $(\lambda^{(l)}, \mu^{(l)})$. We also assume that the solid is under the plane-strain condition. The in-plane displacement u and stress σ are subject to the following two-dimensional Navier-Cauchy equations:

$$\nabla \cdot \sigma + \rho^{(l)} \omega^2 u = 0, \tag{1}$$

where ω is the angular frequency. The stress tensor σ is associated with the displacement u via the following linear relations:

$$\sigma_{ij} = \lambda^{(l)} (\nabla \cdot u) \delta_{ij} + 2\mu^{(l)} \varepsilon_{ij}, \tag{2}$$

$$\varepsilon_{ij} = \frac{1}{2} \left(\frac{\partial u_i}{\partial x_j} + \frac{\partial u_j}{\partial x_i} \right), \tag{3}$$

where δ_{ij} is the Kronecker delta. The displacement u and the normal component $\sigma \cdot n$ of the stress are continuous on the solid–solid interfaces, where n is the unit normal vector.

In what follows, we assume that the solid is a cylinder, i.e., the cross section $\Omega^{(l)}$ of Layer l is given by $\Omega^{(l)} = \{x \in \mathbb{R}^2 \mid R^{(l-1)} < |x| < R^{(l)}\}$ with outer radius $R^{(l)}$ ($R^{(0)} = 0$).

A solution of the Navier-Cauchy Eq. (1) can be sought via Lamé potentials $\phi^{(l)}$ and $\psi^{(l)}$ defined as

$$u_i = \frac{\partial \phi^{(l)}}{\partial x_i} + e_{3ij} \frac{\partial \psi^{(l)}}{\partial x_j} \quad \text{in } \Omega^{(l)}, \tag{4}$$

where e_{ijk} is the Levi-Civita symbol [43]. The potentials decompose the Navier-Cauchy Eq. (1) into the following Helmholtz equations:

$$\nabla^2 \phi^{(l)} + \left(\omega / c_L^{(l)} \right)^2 \phi^{(l)} = 0 \quad \text{in } \Omega^{(l)}, \tag{5}$$

$$\nabla^2 \psi^{(l)} + \left(\omega / c_T^{(l)} \right)^2 \psi^{(l)} = 0 \quad \text{in } \Omega^{(l)}, \tag{6}$$

where $c_L^{(l)} = \sqrt{(\lambda^{(l)} + 2\mu^{(l)})/\rho^{(l)}}$ and $c_T^{(l)} = \sqrt{\mu^{(l)}/\rho^{(l)}}$ are the phase speed of the longitudinal and transverse waves in $\Omega^{(l)}$, respectively. We can write a solution $(\phi^{(l)}, \psi^{(l)})$ as

follows for each azimuthal index $m \in \mathbb{Z}$:

$$\phi^{(l)} = A_L^{(l)} J_m \left(\omega r / c_L^{(l)} \right) \exp(im\theta)$$
$$+ B_L^{(l)} H_m^{(1)} \left(\omega r / c_L^{(l)} \right) \exp(im\theta), \tag{7}$$

$$\psi^{(l)} = A_T^{(l)} J_m \left(\omega r / c_T^{(l)} \right) \exp(im\theta)$$
$$+ B_T^{(l)} H_m^{(1)} \left(\omega r / c_T^{(l)} \right) \exp(im\theta), \tag{8}$$

where (r, θ) is the polar coordinate system. For $l = 1, \ldots, N - 1$, the continuity at the interface $r = R^{(l)}$ associates the unknown coefficients $A_L^{(l)}$, $A_T^{(l)}$, $B_L^{(l)}$, and $B_T^{(l)}$ as

$$M^{(l+1)}(R^{(l)}) \begin{pmatrix} A_L^{(l+1)} \\ A_T^{(l+1)} \\ B_L^{(l+1)} \\ B_T^{(l+1)} \end{pmatrix} = M^{(l)}(R^{(l)}) \begin{pmatrix} A_L^{(l)} \\ A_T^{(l)} \\ B_L^{(l)} \\ B_T^{(l)} \end{pmatrix}, \tag{9}$$

where the matrix $M^{(l)}(R) \in \mathbb{C}^{4 \times 4}$ is dependent on the frequency ω, azimuthal index m, and material constants $\rho^{(l)}, \lambda^{(l)}, \mu^{(l)}$. The explicit form of $M^{(l)}(R)$ is presented in Appendix A. Equation (9) indicates that the matrix $(M^{(l+1)}(R^{(l)}))^{-1} M^{(l)}(R^{(l)})$ is the transfer matrix from Layer l to $l + 1$. Any solution should be bounded at $r = 0$; thus, we have $B_L^{(1)} = B_T^{(1)} = 0$. Accordingly, we can define a 4×2 matrix X that gives

$$X \begin{pmatrix} A_L^{(1)} \\ A_T^{(1)} \end{pmatrix} = \begin{pmatrix} A_L^{(N)} \\ A_T^{(N)} \\ B_L^{(N)} \\ B_T^{(N)} \end{pmatrix}. \tag{10}$$

A. Solid background

First, we formulate a radiation behavior in the background $r > R^{(N)}$. When the background medium is an elastic medium with a mass density ρ and Lamé constants (λ, μ), we define two potentials ϕ and ψ as follows in an analogous manner:

$$u_i = \frac{\partial \phi}{\partial x_i} + e_{3ij} \frac{\partial \psi}{\partial x_j} \quad r > R^{(N)}. \tag{11}$$

We are interested in a radiating field that satisfies the Kupradze–Sommerfeld condition; therefore, the potentials ϕ and ψ are written as

$$\phi = B_L^{BG} H_m^{(1)} (\omega r / c_L) \exp(im\theta), \tag{12}$$

$$\psi = B_T^{BG} H_m^{(1)} (\omega r / c_T) \exp(im\theta), \tag{13}$$

where B_L^{BG} and B_T^{BG} are constants, and c_L and c_T are defined by $c_L = \sqrt{(\lambda + 2\mu)/\rho}$ and $c_T = \sqrt{\mu/\rho}$, respectively. Similar to Eq. (9), the continuity conditions at $r = R^{(N)}$ equate the coefficients as

$$Y_s \begin{pmatrix} B_L^{BG} \\ B_T^{BG} \end{pmatrix} = Z_s \begin{pmatrix} A_L^{(N)} \\ A_T^{(N)} \\ B_L^{(N)} \\ B_T^{(N)} \end{pmatrix}, \tag{14}$$

where the 4×2 matrix Y_s is defined in Appendix A, and $Z_s = M^{(N)}(R^{(N)})$. Equations (10) and (14) give the following linear equations:

$$[Z_s X \quad -Y_s] \begin{pmatrix} A_L^{(1)} \\ A_T^{(1)} \\ B_L^{BG} \\ B_T^{BG} \end{pmatrix} = \begin{pmatrix} 0 \\ 0 \\ 0 \\ 0 \end{pmatrix}. \tag{15}$$

B. Fluid background

The fluid background can be modeled in a similar fashion. Let p be a pressure field that satisfies

$$\nabla^2 p + (\omega/c)^2 p = 0, \quad r > R^{(N)}, \tag{16}$$

where the sound speed c is given by the mass density ρ and bulk modulus κ of the background fluid as $c = \sqrt{\kappa/\rho}$. In analogy with the elastic case, due to the Sommerfeld radiation condition, the pressure p admits the following solution with a constant B^{BG}:

$$p = B^{BG} H_m^{(1)}(\omega r/c) \exp(im\theta), \quad r > R^{(N)}. \tag{17}$$

Elastic-acoustic coupling is established via the continuity of the displacement and traction at $r = R^{(N)}$:

$$\sigma \cdot n = -pn, \tag{18}$$

$$u \cdot n = \frac{1}{\rho\omega^2} \nabla p \cdot n. \tag{19}$$

Using the polar coordinate system, these conditions are translated into

$$Y_f B^{BG} = Z_f \begin{pmatrix} A_L^{(N)} \\ A_T^{(N)} \\ B_L^{(N)} \\ B_T^{(N)} \end{pmatrix}, \tag{20}$$

where the 3×1 matrix Y_f and 3×4 matrix Z_f are given in Appendix A.

Finally, we use Eqs. (10) and (20) to obtain

$$[Z_f X \quad -Y_f] \begin{pmatrix} A_L^{(1)} \\ A_T^{(1)} \\ B^{BG} \end{pmatrix} = \begin{pmatrix} 0 \\ 0 \\ 0 \end{pmatrix}. \tag{21}$$

III. EXCEPTIONAL POINTS

Without any excitation, the time-harmonic oscillation of the multilayered solid is characterized by either Eq. (15) or Eq. (21). These linear systems always have a trivial solution (i.e., uniformly $u = 0$) and possibly nontrivial solutions for discrete angular frequencies $\omega \in \mathbb{C}$ when the determinant of the coefficient matrices becomes zero. These (angular) frequencies are often called quasinormal mode frequencies, complex eigenvalues, or scattering poles. The imaginary part of a scattering pole represents the reciprocal of the lifetime of the corresponding resonance, i.e., exponential decay rate in time induced by the radiation.

The scattering poles are dependent on the system parameters, e.g., the radii and material constants of the layered structure. When two (or more) scattering poles and corresponding resonant modes simultaneously coalesce on the complex ω plane for certain system parameters, the parameters are called an exceptional point on the parameter space.

In contrast to typical non-Hermitian systems, the open systems lack explicit parameters that quantify energy loss. This is because the radiation conditions are equivalent to distributing material loss (i.e., imaginary part of the elastic constants) $\varepsilon > 0$ uniformly in the unbounded background $r > R^{(N)}$ and taking the limit $\varepsilon \downarrow 0$. This limiting absorption principle means that the amount of energy loss per volume (area) is infinitesimal; however, it still yields a certain amount of energy loss in total because the medium is infinitely large. As we are taking the limits $\varepsilon \downarrow 0$ and $r \to \infty$, our formulation eliminates explicit parameters that cause the systems to be non-Hermitian. Nevertheless, the system is non-Hermitian due to the intrinsic radiation loss.

In this study, we show that the multilayered elastic systems exhibit EPs using an optimization algorithm.

To prove that the systems exhibit an EP, we first numerically seek a nontrivial solution of the linear systems Eq. (15) and Eq. (21). The coefficient matrices depend on ω nonlinearly; hence, this is a nonlinear eigenvalue problem in terms of ω. We solve this nonlinear eigenvalue problem using the Sakurai–Sugiura method [44]. Accordingly, we formally write the nonlinear eigenvalue problem as $\mathcal{A}(\omega)\xi = 0$, where $\mathcal{A}$ is a matrix-valued function. The Sakurai-Sugiura method converts the nonlinear eigenvalue problem into a linear one using contour integrals $\int_\gamma W^H \mathcal{A}^{-1}(\omega)V d\omega$ for some full-rank matrices W and V. The linear problem is then solved by a standard eigenvalue solver, which yields the complex eigenvalues (matrix poles) of $\mathcal{A}$ inside the contour path γ and corresponding right eigenvector ξ. For more details, see [44]. A PYTHON implementation is provided on GitHub [45].

Given M scattering poles ω_i ($i = 1, \ldots, M$), we solve the following optimization problem:

$$\min_{\zeta \in \mathcal{P}} J(\zeta) = \sum_{i \neq j} |\omega_i(\zeta) - \omega_j(\zeta)|^2, \tag{22}$$

where $\mathcal{P}$ denotes a parameter space. A solution ζ is an EP of order M in $\mathcal{P}$ if the optimization attains $J = 0$ (i.e., $\omega_1 = \ldots = \omega_M$), and all the corresponding resonant modes are identical.

IV. RESULTS AND DISCUSSION

A. Solid background

In this subsection, we will show that the solid-solid system exhibits second- and third-order EPs. First, we consider the double-layered solid ($N = 2$) embedded in a background medium with (ρ, λ, μ). In analogy with optical layered systems [18], we expect that non-Hermitian degeneracy is achieved when two whispering gallary modes coalesce at the same frequency. This can be accomplished when the refractive index of $\Omega^{(1)}$ is larger than that of $\Omega^{(2)}$. In what follows, we limit the consideration to the case of $m = \pm 8$. Poisson's ratio $\nu^{(l)}$ is uniformly 0.3 for all elastic media. Figure 2 shows the distribution of the scattering
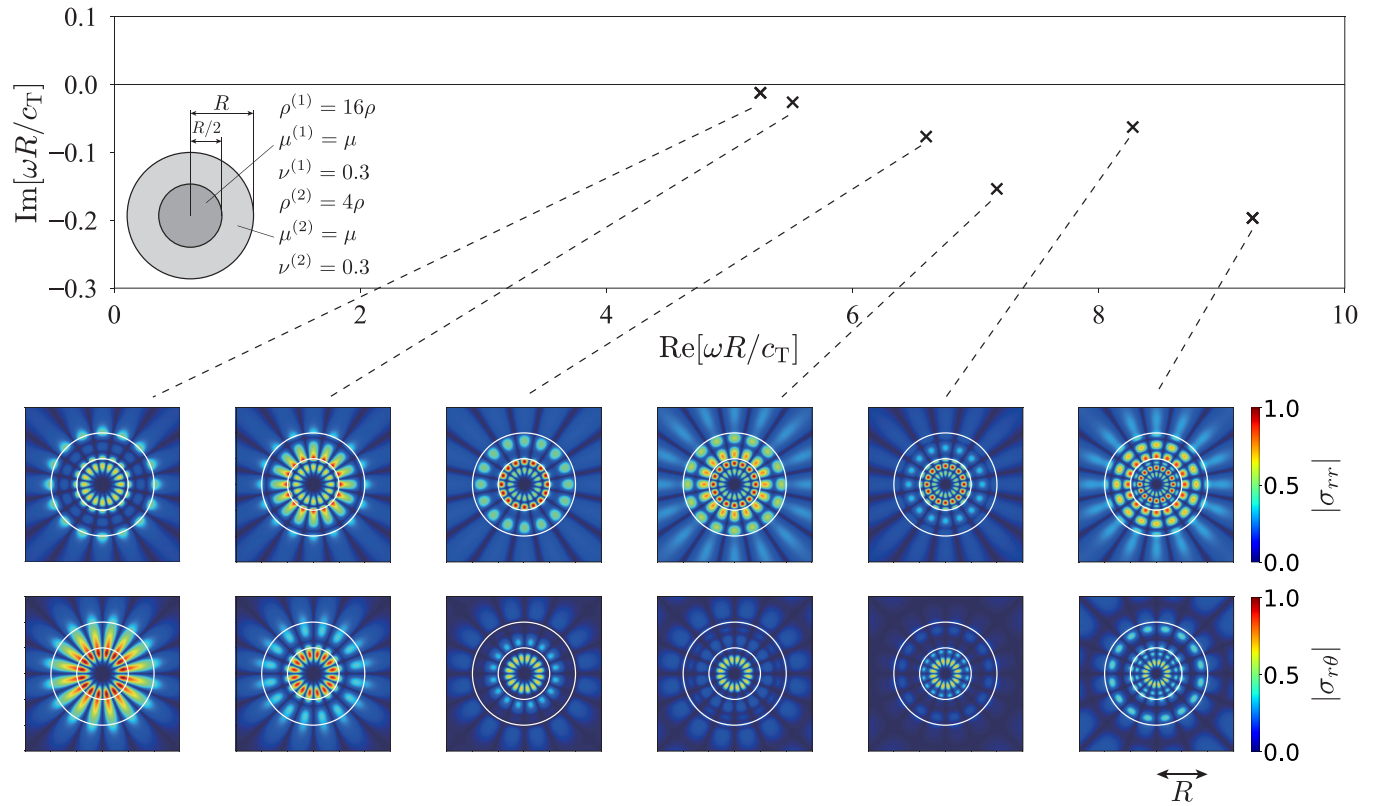
FIG. 2. Scattering poles and corresponding resonant modes of the double layers in the solid background. The top figure shows the distibution of some scattering poles computed by solving the nonlinear eigenvalue problem Eq. (15) numerically. The corresponding resonant modes are illustrated in the bottom.

poles and corresponding resonant modes for $\rho^{(1)} = 16\rho$, $\rho^{(2)} = 4\rho$, $\mu^{(1)} = \mu^{(2)} = \mu$, and $R^{(2)} = 2R^{(1)} =: R$. The result clearly indicates that the multilayered elastic system exhibits whispering gallary modes around the solid interfaces. Furthermore, we observe no scattering pole degeneracy for the prescribed parameters. We focus herein on the two neighboring scattering poles, $\omega_1 R/c_T = 5.2513 - 0.012416i$ and $\omega_2 R/c_T = 5.5130 - 0.026387i$, and seek a second-order EP on the $R^{(1)}$–$\rho^{(1)}$ parameter plane. We performed a two-variable optimization using the Nelder–Mead method [46] and found an optimal solution $R^{(1)}/R = 0.34811$ and $\rho^{(1)}/\rho = 35.054$. This optimized system has two scattering poles at $\omega R/c_T = 5.37067922 - 0.01744497i$, $5.37067926 - 0.01744494i$. The corresponding resonant modes, shown in Fig. 3(b), also coalesce at the parameters. The simultaneous degeneracy of the poles and resonant modes is a proof of the existence of a second-order EP. The unique characteristics of second-order EPs can be confirmed by encircling them on a two-variable parameter space. Figure 3(a) defines a closed elliptic path on the $R^{(1)}$–$\rho^{(1)}$ plane. The center of the path is the obtained EP. By tracing the path counterclockwise, we compute the two scattering poles on the complex ω plane and plot their trajectories in Fig. 3(c). The results show that a single pole does not form a closed path on the ω-plane although the parameter curve does on the $R^{(1)} - \rho^{(1)}$ plane. Instead, the pair of the two poles closes the trajectory. Equivalently, a single pole forms a closed loop when the parameter curve encircles the EP twice. This feature is analogous to the multivalued square root function on the complex plane.

We discuss this square rootlike behavior by computing the pole pair for various parameters $R^{(1)}$ and $\rho^{(1)}$ around the EP. Figure 4 illustrates the result. The pair forms two crossed sheets that branch off at the EP. This structure is similar to the Riemann surfaces of the square root function. These results imply that the obtained EP originates from a branch point of a complex-valued function, although it is not explicit in Eq. (15).

We now show that a triple-layered solid exhibits a third-order EP by starting with the following parameters:

(1) mass density $\rho^{(1)} = 64\rho$, $\rho^{(2)} = 16\rho$, $\rho^{(3)} = 4\rho$;

(2) shear modulus $\mu^{(1)} = \mu^{(2)} = \mu^{(3)} = \mu$;

(3) radii $R^{(1)} = R/4$, $R^{(2)} = R/2$, $R^{(3)} =: R$.

We chose three scattering poles $\omega R/c_T = 5.2088 - 0.005504i$, $5.3657 - 0.016873i$, and $5.5851 - 0.017023i$ and optimized the five parameters $R^{(1)}$, $R^{(2)}$, $\rho^{(1)}$, $\rho^{(2)}$, and $\rho^{(3)}$ to find an EP.

The optimized parameters are $R^{(1)}/R = 0.11969$, $R^{(2)}/R = 0.38351$, $\rho^{(1)}/\rho = 270.69$, $\rho^{(2)}/\rho = 25.971$, and $\rho^{(3)}/\rho = 3.57568$. The optimized system has three poles $\omega R/c_T$ at $5.6385 - 0.019254i$, $5.6387 - 0.019293i$, and $5.6386 - 0.019242i$, which are almost degenerated. Moreover, Fig. 5(b) show that not only the pole values but also corresponding resonant modes coalesced at the point. We confirm that the degeneracy arose from a third-order EP by performing the EP encircling on the $R^{(2)}$–$\rho^{(2)}$ parameter space. Namely, we continuously change the values of $R^{(2)}$ and $\rho^{(2)}$ and calculate the poles on the complex ω-plane while the other parameters remain fixed.
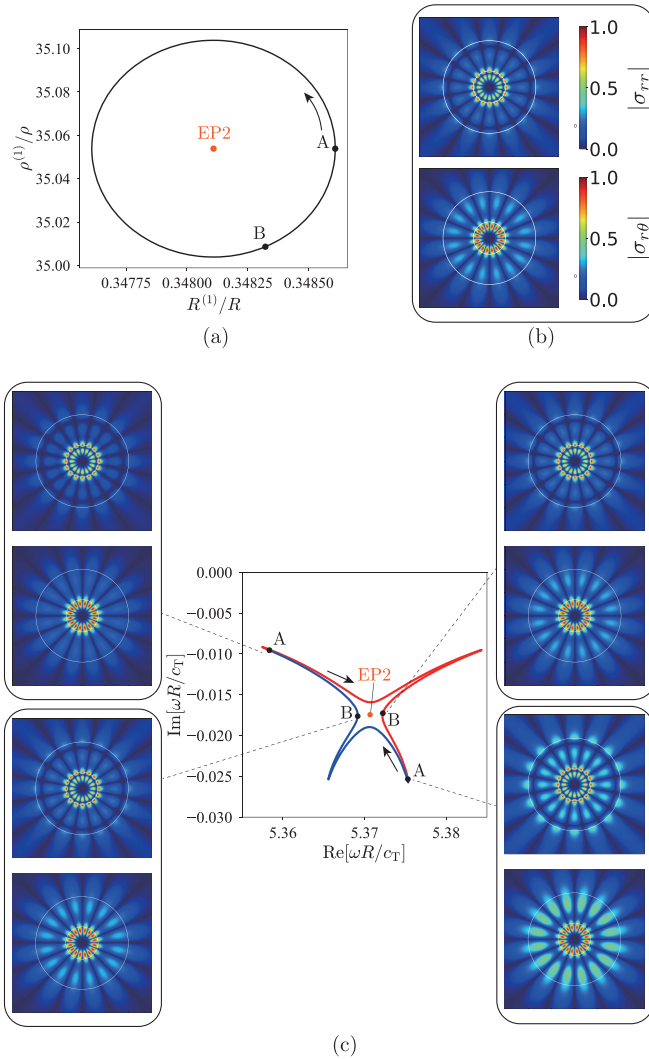
(a)

(b)

(c)

FIG. 3. Encircling a second-order EP (EP2) in the solid-solid system. (a) Encircling path in the parameter space. We change the parameters $R^{(1)}$ and $\rho^{(1)}$ continuously along the path and compute the corresponding scattering poles. For each pair of the parameters, the corresponding scattering poles are computed by numerically solving the nonlinear eigenvalue problem Eq. (15). (b) Degenerate resonant mode at the EP2. (c) Trajectory of the two scattering poles. Each color corresponds to a single encircling shown in (a).

Figure 5 depicts the results. As with the previous discussion on the second-order EP, we move the two parameters counterclockwise along the elliptic path shown in Fig. 5(a). Figure 5(c) plots the trajectories of the three poles. The three trajectories form a single closed curve, which is a well-known characteristic of third-order EPs. Another important property is the asymptotic behavior of the degenerate poles when the parameters are perturbed at the third-order EP. We fix the parameter $\rho^{(2)}$ at the EP and perturb the other parameter as $R^{(2)} = 0.38351R + \Delta_R$, where Δ_R is sufficiently small. The three poles should deviate from the degenerate value as the value of Δ_R increases. We define the variation as $\Delta_\omega = \max_{i \neq j} |\omega_i - \omega_j|$, which is a function of Δ_R, and plot its values in Fig. 6. The result shows that the variation asymptotically behaves as $O(\Delta_R^{1/3})$, while the second-order EP exhibits the
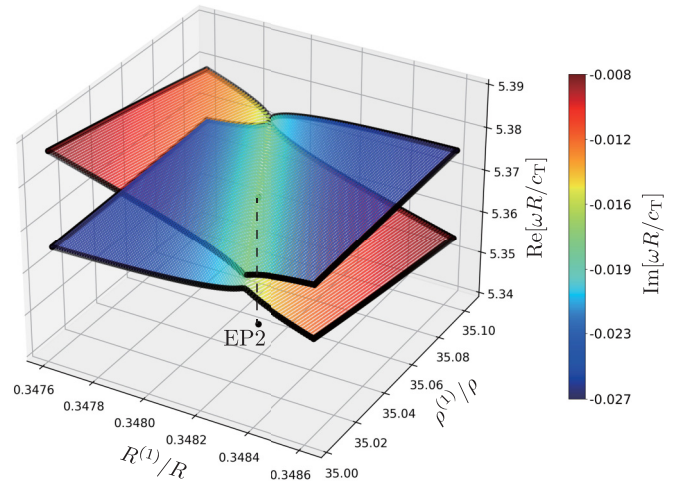

FIG. 4. Real and imaginary parts of the scattering poles for various parameters $R^{(1)}$ and $\rho^{(1)}$ around the EP2.

square-root behavior. This is another characteristic of third-order EPs.

B. Fluid background

When the layered solid is immersed in a fluid medium, the system loses its energy due to the acoustic wave radiation. Here, we use the same optimization approach to show that the solid-fluid coupled systems exhibit EPs.

In this section, we fix the mass density $\rho > 0$, bulk modulus $\kappa > 0$, and outer radius $R^{(N)} =: R$. We first assume $N = 2$ and compute the scattering poles for $\rho^{(1)} = 16\rho$, $\rho^{(2)} = 4\rho$, $\mu^{(1)} = \mu^{(2)} = \kappa$, and $R^{(1)} = R/2$. Subsequently, we chose two scattering poles $\omega R/c$ at $6.4436 - 0.029230i$ and $7.0062 - 0.035093i$ and optimize the parameters $\rho^{(1)}$ and $R^{(1)}$. Figure 7 shows the results of the optimization and EP encircling. The parameter optimization successfully minimizes the objective function J with two poles $\omega R/c$ at $6.5056469 - 0.0240559i$ and $6.5056469 - 0.0240557i$. The degenerate resonant modes are plotted in Fig. 7(b). Encircling the obtained parameters $R^{(1)}/R = 0.29400$ and $\rho^{(1)}/\rho = 54.145$ on the $R^{(1)}-\rho^{(1)}$ plane as shown in Fig. 7(a), we obtain the trajectories of the two poles on the complex ω plane [Fig. 7(c)] with the same structures as the second-order EP of the solid-solid model. From the results, we conclude that a second-order EP exists within the parameter path. Finally, we shall prove the existence of a third-order EP. As with the solid-solid model, we use the triple-layered solid ($N = 3$) with the following parameters:

(1) mass density $\rho^{(1)} = 64\rho$, $\rho^{(2)} = 16\rho$, $\rho^{(3)} = 4\rho$;
(2) shear modulus $\mu^{(1)} = \mu^{(2)} = \mu^{(3)} = \kappa$;
(3) radii $R^{(1)} = R/4$, $R^{(2)} = R/2$, $R^{(3)} =: R$.

The system has three scattering poles $\omega R/c$ at $6.4222 - 0.022268i$, $6.7600 - 0.025502i$, and $7.2757 - 0.019004i$. We optimize the parameters $R^{(1)}$, $R^{(2)}$, $\rho^{(1)}$, $\rho^{(2)}$, and $\rho^{(3)}$ with the other parameters fixed. Fig. 8 illustrates the results. The three poles almost coalesce at $R^{(1)}/R = 0.12678$, $R^{(2)}/R = 0.40343$, $\rho^{(1)}/\rho = 200.46$, $\rho^{(2)}/\rho = 19.400$, and $\rho^{(3)}/\rho = 2.7136$ with $\omega_1 R/c = 7.7966 - 0.094927i$, $\omega_2 R/c = 7.7971 - 0.094901i$, and
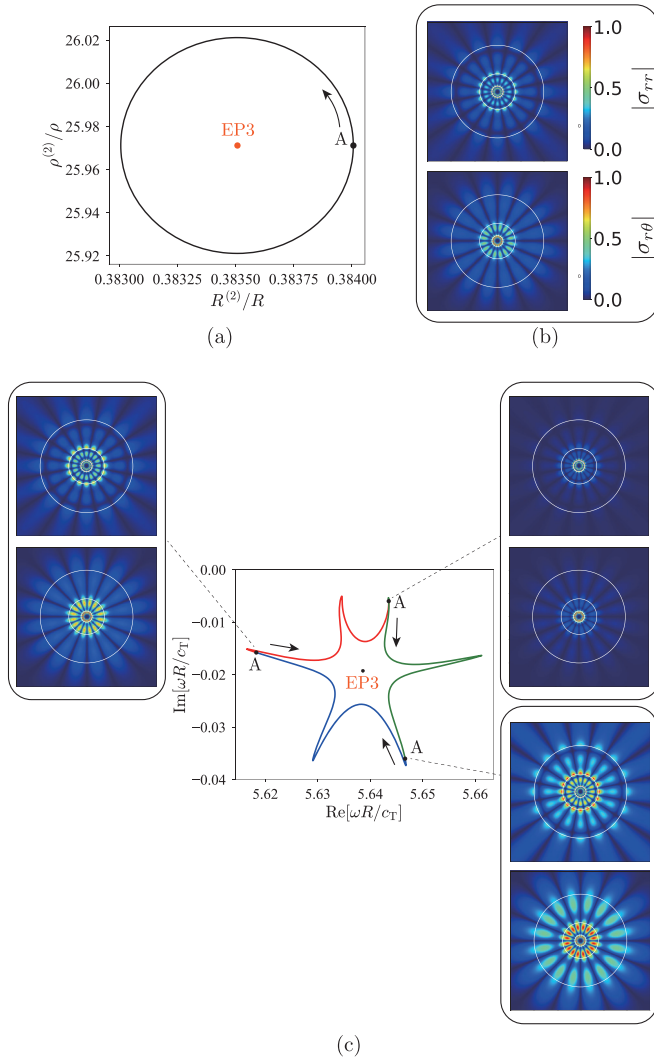
FIG. 5. Encircling a third-order EP (EP3) in the solid-solid system. (a) Encircling path in the parameter space. We change the parameters $R^{(2)}$ and $\rho^{(2)}$ continuously along the path and compute the corresponding scattering poles. For each pair of the parameters, the corresponding scattering poles are computed by numerically solving the nonlinear eigenvalue problem Eq. (15). (b) Degenerate resonant mode at the EP3. (c) Trajectory of the two scattering poles. Each color corresponds to the single encircling shown in (a).
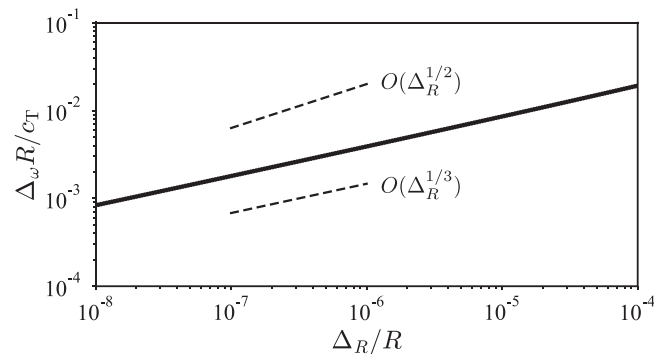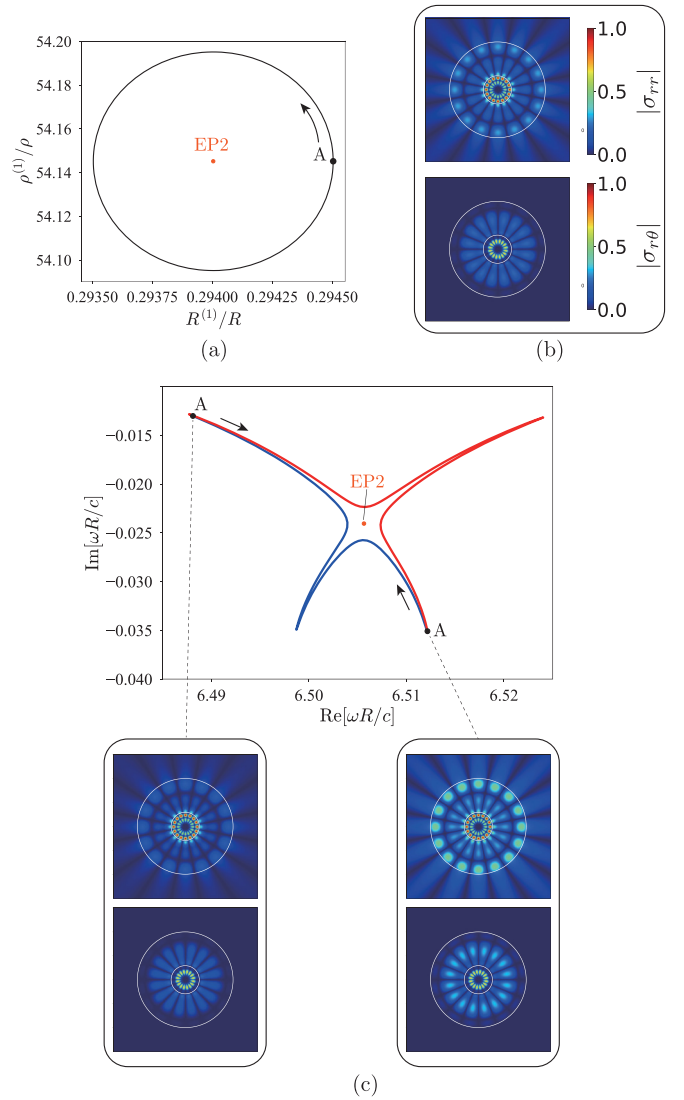

FIG. 7. Encircling a second-order EP (EP2) in the solid–fluid system. (a) Encircling path in the parameter space. We change the parameters $R^{(1)}$ and $\rho^{(1)}$ continuously along the path and compute the corresponding scattering poles. For each pair of the parameters, the corresponding scattering poles are computed by numerically solving the nonlinear eigenvalue problem Eq. (21). (b) Degenerate resonant mode at the EP2. (c) Trajectory of the two scattering poles. Each color corresponds to the single encircling shown in (a).

$\omega_3 R/c = 7.7968 - 0.094903i$. Their resonant modes are also degenerated as shown in Fig. 8(b). The existence of a third-order EP is confirmed by the EP encircling. Figures 8(a) and 8(c) present the results of the EP encircling. Like the solid-solid case (Fig. 5), we observe a threefold structure on the complex ω plane, which implies the existence of a three-order EP.

The numerical results suggest that radiating acoustic and elastic waves induce the non-Hermiticity and realize second- and third-order EPs. We observe no significant differences between EPs in the solid and fluid backgrounds, e.g., resonant modes, behavior of the scattering poles during the EP encircling, and their sensitivity. From a practical perspective, the solid–fluid system is easier to fabricate because we need

FIG. 6. Variation of the degenerate poles at the third-order EP when the parameter $R^{(2)}$ is perturbed.
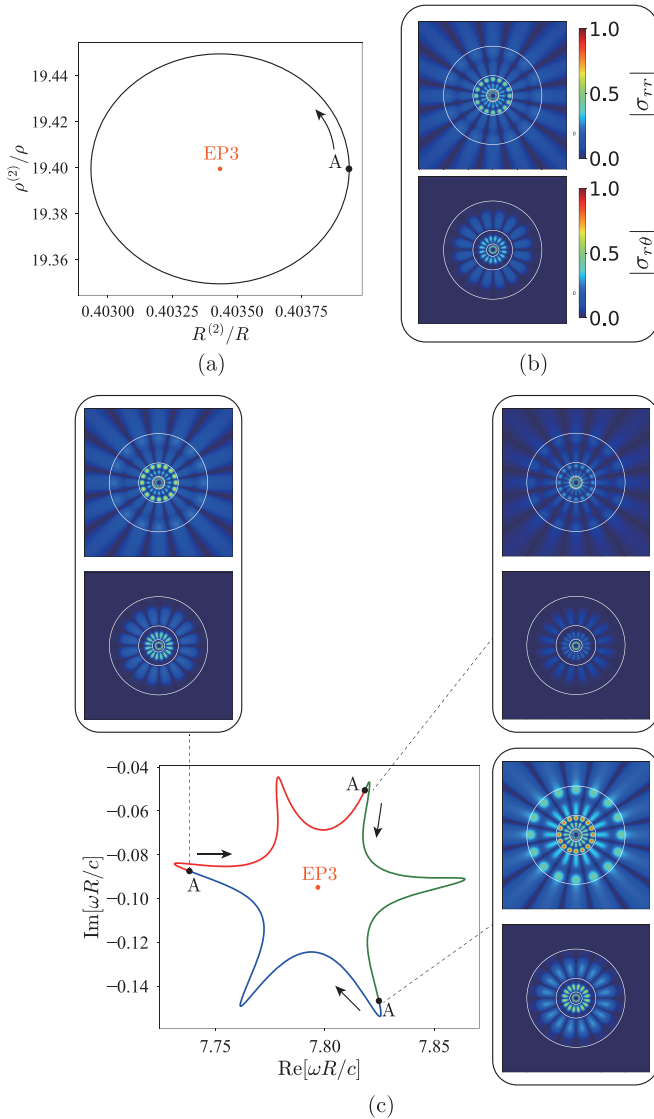
FIG. 8. Encircling a third-order EP (EP3) in the solid-fluid system. (a) Encircling path in the parameter space. We change the parameters $R^{(2)}$ and $\rho^{(2)}$ continuously along the path and compute the corresponding scattering poles. For each pair of the parameters, the corresponding scattering poles are computed by numerically solving the nonlinear eigenvalue problem Eq. (21). (b) Degenerate resonant mode at the EP3. (c) Trajectory of the two scattering poles. Each color corresponds to a single encircling shown in (a).

a sufficiently large medium with small viscosity surrounding the multilayered solid to utilize the radiation effect. In the next subsection, we discuss a potential application of the proposed systems.

C. Potential application and experimental platform

A promising application of the scattering pole degeneracy is the highly sensitive detection of inhomogeneity and defects in the vicinity of the system as the $O(\Delta^{1/2})$ or $O(\Delta^{1/3})$ sensitivity exaggerates the variation of spectral properties, where Δ denotes a parameter change. To this end, we need to measure scattering poles experimentally. Scattering poles are associated with transient scattering properties of an open
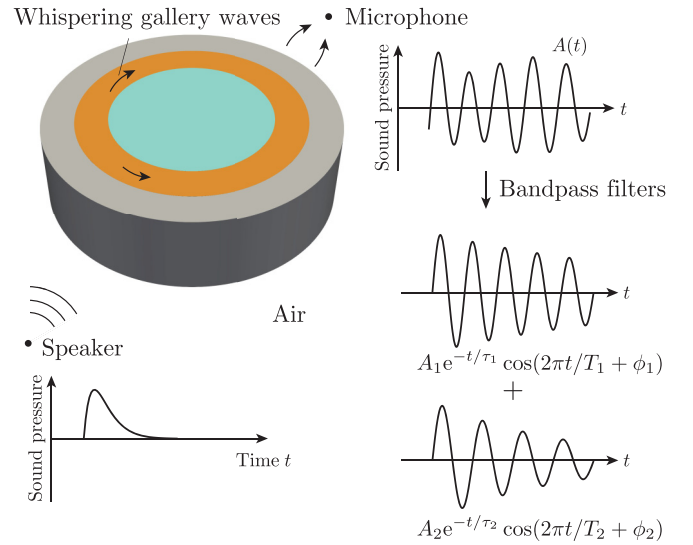

FIG. 9. Experimental setup. Two scattering poles ω_1 and ω_2 are measured from the sound pressure $A(t)$ during a transient scattering process. Each pole ω_j is calculated from the period $T_j > 0$ and lifetime $\tau_j > 0$ of a damped oscillation as $\omega_j = 2\pi/T_j - \mathrm{i}/\tau_j$.

system, i.e., after a sufficient amount of time has elapsed, a transient acoustic field $A(t)$ at a fixed point in space with time t is expanded as

$$A(t) \simeq \sum_j A_j e^{-t/\tau_j} \cos(2\pi t/T_j + \phi_j), \qquad (23)$$

where A_j and ϕ_j are constants. The time period $T_j > 0$ and lifetime $\tau_j > 0$ give a scattering pole as $\omega_j = 2\pi/T_j - \mathrm{i}/\tau_j$. This means that each scattering pole can be experimentally identified once the corresponding period T_j and lifetime τ_j are measured. Thus precise measurements of T_i and τ_i are essential to realize highly sensitive mechanical sensors. This process is schematically illustrated in Fig. 9.

V. CONCLUSIONS

This study discussed the non-Hermitian degeneracy of the scattering poles in cylindrical elastic systems with radiation loss. We first formulated two-dimensional elastodynamic problems using Lamé potentials and cylindrical functions. Some system parameters were optimized such that two or three scattering poles coalesce on the complex frequency plane. We performed the EP encircling around the optimized parameters to confirm the existence of second- and third-order EPs. We found that the sensitivity of degenerate poles at a third-order EP is $O(\Delta^{1/3})$, where Δ is a system parameter. This anomalous sensitivity allows enhancement on mechanical sensors, such as pressure/stress sensing and defect detection.

APPENDIX: EXPLICIT FORMS OF THE MATRICES

To formulate Eq. (9), we use the continuity of u and $\sigma \cdot n$, which is equivalent to that of u_r, u_θ, σ_{rr}, and $\sigma_{r\theta}$. After some calculations [43], we have

$$
M^{(l)}(r) = \begin{bmatrix} U_1^{(l)}(r) & U_2^{(l)}(r) & \tilde{U}_1^{(l)}(r) & \tilde{U}_2^{(l)}(r) \\ V_1^{(l)}(r) & V_2^{(l)}(r) & \tilde{V}_1^{(l)}(r) & \tilde{V}_2^{(l)}(r) \\ T_{11}^{(l)}(r) & T_{12}^{(l)}(r) & \tilde{T}_{11}^{(l)}(r) & \tilde{T}_{12}^{(l)}(r) \\ T_{41}^{(l)}(r) & T_{42}^{(l)}(r) & \tilde{T}_{41}^{(l)}(r) & \tilde{T}_{42}^{(l)}(r) \end{bmatrix}, \quad \text{(A1)}
$$

where the matrices are defined as

$$
T_{11}^{(l)} = \frac{2\mu^{(l)}}{r^2}\left[\left(m^2 + m - \frac{1}{2}(k_T^{(l)})^2 r^2\right)J_m(k_L^{(l)}r) - k_L^{(l)}rJ_{m-1}(k_L^{(l)}r)\right], \quad \text{(A2)}
$$

$$
T_{12}^{(l)} = \frac{2\mu^{(l)}}{r^2}\left[-im\big((m+1)J_m(k_T^{(l)}r) - k_T^{(l)}rJ_{m-1}(k_T^{(l)}r)\big)\right], \quad \text{(A3)}
$$

$$
T_{41}^{(l)} = \frac{2\mu^{(l)}}{r^2}\left[-im\big((m+1)J_m(k_L^{(l)}r) - k_L^{(l)}rJ_{m-1}(k_L^{(l)}r)\big)\right], \quad \text{(A4)}
$$

$$
T_{42}^{(l)} = \frac{2\mu^{(l)}}{r^2}\left[-\left(m^2 + m - \frac{1}{2}(k_T^{(l)})^2 r^2\right)J_m(k_T^{(l)}r) + k_T^{(l)}rJ_{m-1}(k_T^{(l)}r)\right], \quad \text{(A5)}
$$

$$
U_1^{(l)} = k_L^{(l)}J_m'(k_L^{(l)}r), \quad \text{(A6)}
$$

$$
U_2^{(l)} = \frac{im}{r}J_m(k_T^{(l)}r), \quad \text{(A7)}
$$

$$
V_1^{(l)} = \frac{im}{r}J_m(k_L^{(l)}r), \quad \text{(A8)}
$$

$$
V_2^{(l)} = -k_T^{(l)}J_m'(k_T^{(l)}r), \quad \text{(A9)}
$$

with $k_L^{(l)} = \omega/c_L^{(l)}$ and $k_T^{(l)} = \omega/c_T^{(l)}$. The functions with the tilde are defined by replacing J_m with $H_m^{(1)}$.

Similarly, the matrix Y_s is given by

$$
Y_s = \begin{bmatrix} \tilde{U}_1(R^{(N)}) & \tilde{U}_2(R^{(N)}) \\ \tilde{V}_1(R^{(N)}) & \tilde{V}_2(R^{(N)}) \\ \tilde{T}_{11}(R^{(N)}) & \tilde{T}_{12}(R^{(N)}) \\ \tilde{T}_{41}(R^{(N)}) & \tilde{T}_{42}(R^{(N)}) \end{bmatrix}, \quad \text{(A10)}
$$

where the block matrices are defined by replacing the material parameters $\rho^{(l)}$, $\lambda^{(l)}$, and $\mu^{(l)}$ in $\tilde{U}_i$, $\tilde{V}_i$, and $\tilde{T}_{ij}$ with the background ones ρ, λ, and μ, respectively.

The solid-fluid coupling matrices are written as

$$
Z_f = \begin{bmatrix} T_{11}^{(l)}(R^{(N)}) & T_{12}^{(l)}(R^{(N)}) & \tilde{T}_{11}^{(l)}(R^{(N)}) & \tilde{T}_{12}^{(l)}(R^{(N)}) \\ T_{41}^{(l)}(R^{(N)}) & T_{42}^{(l)}(R^{(N)}) & \tilde{T}_{41}^{(l)}(R^{(N)}) & \tilde{T}_{42}^{(l)}(R^{(N)}) \\ U_1^{(l)}(R^{(N)}) & U_2^{(l)}(R^{(N)}) & \tilde{U}_1^{(l)}(R^{(N)}) & \tilde{U}_2^{(l)}(R^{(N)}) \end{bmatrix}, \quad \text{(A11)}
$$

$$
Y_f = \begin{bmatrix} -H_n^{(1)}(\omega R^{(N)}/c) \\ 0 \\ \frac{1}{c\rho\omega}H_n^{(1)\prime}(\omega R^{(N)}/c) \end{bmatrix}. \quad \text{(A12)}
$$

[1] T. Kato, *Perturbation Theory for Linear Operators*, Classics in Mathematics Vol. 132 (Springer, Berlin, Heidelberg, 1995).

[2] M. Berry, Physics of nonhermitian degeneracies, Czech. J. Phys. **54**, 1039 (2004).

[3] W. D. Heiss, The physics of exceptional points, J. Phys. A: Math. Theor. **45**, 444016 (2012).

[4] C. Dembowski, H.-D. Gräf, H. L. Harney, A. Heine, W. D. Heiss, H. Rehfeld, and A. Richter, Experimental Observation of the Topological Structure of Exceptional Points, Phys. Rev. Lett. **86**, 787 (2001).

[5] J. Wiersig, Enhancing the Sensitivity of Frequency and Energy Splitting Detection by Using Exceptional Points: Application to Microcavity Sensors for Single-Particle Detection, Phys. Rev. Lett. **112**, 203901 (2014).

[6] J. Wiersig, Sensors operating at exceptional points: General theory, Phys. Rev. A **93**, 033809 (2016).

[7] W. Chen, Ş. Kaya Özdemir, G. Zhao, J. Wiersig, and L. Yang, Exceptional points enhance sensing in an optical microcavity, Nature (London) **548**, 192 (2017).

[8] M. P. Hokmabadi, A. Schumer, D. N. Christodoulides, and M. Khajavikhan, Non-Hermitian ring laser gyroscopes with enhanced Sagnac sensitivity, Nature (London) **576**, 70 (2019).

[9] T. Xing, Z. Pan, Y. Tao, G. Xing, R. Wang, W. Liu, E. Xing, J. Rong, J. Tang, and J. Liu, Ultrahigh sensitivity stress sensing method near the exceptional point of parity-time symmetric systems, J. Phys. D **53**, 205102 (2020).

[10] D. Yu, M. Humar, K. Meserve, R. C. Bailey, S. N. Chormaic, and F. Vollmer, Whispering-gallery-mode sensors for biological and physical sensing, Nat. Rev. Meth. Primers **1**, 83 (2021).

[11] J. Yuan, L. Geng, J. Huang, Q. Guo, J. Yang, G. Hu, and X. Zhou, Exceptional Points Induced by Time-Varying Mass to Enhance the Sensitivity of Defect Detection, Phys. Rev. Appl. **18**, 064055 (2022).

[12] S. Klaiman, U. Günther, and N. Moiseyev, Visualization of Branch Points in $\mathcal{PT}$-Symmetric Waveguides, Phys. Rev. Lett. **101**, 080402 (2008).

[13] S. Longhi, Bloch Oscillations in Complex Crystals with $\mathcal{PT}$ Symmetry, Phys. Rev. Lett. **103**, 123601 (2009).

[14] C. E. Rüter, K. G. Makris, R. El-Ganainy, D. N. Christodoulides, M. Segev, and D. Kip, Observation of parity–time symmetry in optics, Nat. Phys. **6**, 192 (2010).

[15] Ş. K. Özdemir, S. Rotter, F. Nori, and L. Yang, Parity–time symmetry and exceptional points in photonics, Nat. Mater. **18**, 783 (2019).

[16] Y. D. Chong, L. Ge, and A. D. Stone, $\mathcal{PT}$-Symmetry Breaking and Laser-Absorber Modes in Optical Scattering Systems, Phys. Rev. Lett. **106**, 093902 (2011).

[17] H. Cao and J. Wiersig, Dielectric microcavities: Model systems for wave chaos and non-Hermitian physics, Rev. Mod. Phys. **87**, 61 (2015).

[18] J. Kullig, C.-H. Yi, M. Hentschel, and J. Wiersig, Exceptional points of third-order in a layered optical microdisk cavity, New J. Phys. **20**, 083016 (2018).

[19] E. Bulgakov, K. Pichugin, and A. Sadreev, Exceptional points in a dielectric spheroid, Phys. Rev. A **104**, 053507 (2021).

[20] A. Abdrabou and Y. Y. Lu, Exceptional points for resonant states on parallel circular dielectric cylinders, J. Opt. Soc. Am. B **36**, 1659 (2019).

[21] S. Gwak, H. Kim, H.-H. Yu, J. Ryu, C.-M. Kim, C.-H. Yi, and C.-H. Yi, Rayleigh scatterer-induced steady exceptional points of stable-island modes in a deformed optical microdisk, Opt. Lett. **46**, 2980 (2021).

[22] B. Zhen, C. W. Hsu, Y. Igarashi, L. Lu, I. Kaminer, A. Pick, S.-L. Chua, J. D. Joannopoulos, and M. Soljačić, Spawning rings of exceptional points out of Dirac cones, Nature (London) **525**, 354 (2015).

[23] P. M. Kamiński, A. Taghizadeh, O. Breinbjerg, J. Mørk, and S. Arslanagić, Control of exceptional points in photonic crystal slabs, Opt. Lett. **42**, 2866 (2017).

[24] A. Abdrabou and Y. Y. Lu, Exceptional points of resonant states on a periodic slab, Phys. Rev. A **97**, 063822 (2018).

[25] H. Zhou, C. Peng, Y. Yoon, C. W. Hsu, K. A. Nelson, L. Fu, J. D. Joannopoulos, M. Soljačić, and B. Zhen, Observation of bulk Fermi arc and polarization half charge from paired exceptional points, Science **359**, 1009 (2018).

[26] A. Abdrabou and Y. Y. Lu, Exceptional points of Bloch eigenmodes on a dielectric slab with a periodic array of cylinders, Phys. Scr. **95**, 095507 (2020).

[27] X. Zhu, H. Ramezani, C. Shi, J. Zhu, and X. Zhang, $\mathcal{PT}$-Symmetric Acoustics, Phys. Rev. X **4**, 031042 (2014).

[28] R. Fleury, D. Sounas, and A. Alù, An invisible acoustic sensor based on parity-time symmetry, Nat. Commun. **6**, 5905 (2015).

[29] R. Fleury, D. L. Sounas, and A. Alù, Parity-time symmetry in acoustics: Theory, devices, and potential applications, IEEE J. Sel. Top. Quantum Electron. **22**, 121 (2016).

[30] C. Shi, M. Dubois, Y. Chen, L. Cheng, H. Ramezani, Y. Wang, and X. Zhang, Accessing the exceptional points of parity-time symmetric acoustics, Nat. Commun. **7**, 11110 (2016).

[31] J. Christensen, M. Willatzen, V. R. Velasco, and M.-H. Lu, Parity-Time Synthetic Phononic Media, Phys. Rev. Lett. **116**, 207601 (2016).

[32] V. Achilleos, G. Theocharis, O. Richoux, and V. Pagneux, Non-Hermitian acoustic metamaterials: Role of exceptional points in sound absorption, Phys. Rev. B **95**, 144303 (2017).

[33] Y. Aurégan and V. Pagneux, $\mathcal{PT}$-Symmetric Scattering in Flow Duct Acoustics, Phys. Rev. Lett. **118**, 174301 (2017).

[34] Z. Hou, H. Ni, and B. Assouar, $\mathcal{PT}$-Symmetry for Elastic Negative Refraction, Phys. Rev. Appl. **10**, 044071 (2018).

[35] Q. Wu, Y. Chen, and G. Huang, Asymmetric scattering of flexural waves in a parity-time symmetric metamaterial beam, J. Acoust. Soc. Am. **146**, 850 (2019).

[36] X. Wang, X. Fang, D. Mao, Y. Jing, and Y. Li, Extremely Asymmetrical Acoustic Metasurface Mirror at the Exceptional Point, Phys. Rev. Lett. **123**, 214302 (2019).

[37] V. Domínguez-Rocha, R. Thevamaran, F. M. Ellis, and T. Kottos, Environmentally Induced Exceptional Points in Elastodynamics, Phys. Rev. Appl. **13**, 014060 (2020).

[38] M. I. N. Rosa, M. Mazzotti, and M. Ruzzene, Exceptional points and enhanced sensitivity in PT-symmetric continuous elastic media, J. Mech. Phys. Solids **149**, 104325 (2021).

[39] M. Farhat, P.-Y. Chen, S. Guenneau, and Y. Wu, Self-dual singularity through lasing and antilasing in thin elastic plates, Phys. Rev. B **103**, 134101 (2021).

[40] R. Cai, Y. Jin, Y. Li, T. Rabczuk, Y. Pennec, B. Djafari-Rouhani, and X. Zhuang, Exceptional Points and Skin Modes in Non-Hermitian Metabeams, Phys. Rev. Appl. **18**, 014067 (2022).

[41] J. Yi, Z. Ma, R. Xia, M. Negahban, C. Chen, and Z. Li, Structural periodicity dependent scattering behavior in parity-time symmetric elastic metamaterials, Phys. Rev. B **106**, 014303 (2022).

[42] A. A. Mokhtari, Y. Lu, Q. Zhou, A. V. Amirkhizi, and A. Srivastava, Scattering of in-plane elastic waves at metamaterial interfaces, Int. J. Eng. Sci. **150**, 103278 (2020).

[43] A. C. Eringen and E. S. Suhubi, *Elastodynamics, Vol. II, Linear Theory* (Academic Press, New York, 1975).

[44] J. Asakura, T. Sakurai, H. Tadano, T. Ikegami, and K. Kimura, A numerical method for nonlinear eigenvalue problems using contour integrals, JSIAM Letters **1**, 52 (2009).

[45] K. Matsushima, https://github.com/k-matsushima-19/scattering-pole-elasticity (2023).

[46] F. Gao and L. Han, Implementing the Nelder-Mead simplex algorithm with adaptive parameters, Comput. Optim. Appl. **51**, 259 (2012).